TISSUE ENGINEERING: Part A
Volume 21, Numbers 13 and 14, 2015

DOI: 10.1089/ten.tea.2015.0019

Positively Charged Oligo[Poly(Ethylene Glycol) Fumarate] Scaffold Implantation Results in a Permissive Lesion Environment after Spinal Cord Injury in Rat

Jeffrey S. Hakim, BS,[1,2] Melika Esmaeili Rad, BS,[2] Peter J. Grahn, BA,[2] Bingkun K. Chen, MD, PhD,[3] Andrew M. Knight, PhD,[3] Ann M. Schmeichel, AS,[3] Nasro A. Isaq, BS,[2] Mahrokh Dadsetan, PhD,[1,4] Michael J. Yaszemski, MD, PhD,[1,4,5] and Anthony J. Windebank, MD[1,3,5]

Positively charged oligo[poly(ethylene glycol) fumarate] (OPF+) scaffolds loaded with Schwann cells bridge spinal cord injury (SCI) lesions and support axonal regeneration in rat. The regeneration achieved is not sufficient for inducing functional recovery. Attempts to increase regeneration would benefit from understanding the effects of the scaffold and transplanted cells on lesion environment. We conducted morphometric and stereological analysis of lesions in rats implanted with OPF+ scaffolds with or without loaded Schwann cells 1, 2, 3, 4, and 8 weeks after thoracic spinal cord transection. No differences were found in collagen scarring, cyst formation, astrocyte reactivity, myelin debris, or chondroitin sulfate proteoglycan (CSPG) accumulation. However, when scaffold-implanted animals were compared with animals with transection injuries only, these barriers to regeneration were significantly reduced, accompanied by increased activated macrophages/microglia. This distinctive and regeneration permissive tissue reaction to scaffold implantation was independent of Schwann cell transplantation. Although the tissue reaction was beneficial in the short term, we observed a chronic fibrotic host response, resulting in scaffolds surrounded by collagen at 8 weeks. This study demonstrates that an appropriate biomaterial scaffold improves the environment for regeneration. Future targeting of the host fibrotic response may allow increased axonal regeneration and functional recovery.

Introduction

Spinal cord injury (SCI) has an incidence of 12,000 to 20,000 new cases per year in the United States, with nearly a quarter of a million Americans living with the condition.[1] However, there are currently no therapies to ameliorate the neurological impairments resulting from SCI. The central nervous system (CNS) is very limited in its natural regenerative capacity following SCI. This lack of regeneration results from the inhibitory environment that develops at the lesion site following SCI and a diminished intrinsic capacity for adult CNS axons to initiate growth programs.[2] The environment that prohibits regeneration has an overall biological advantage because it inhibits structural remodeling of the mature nervous system after it has formed appropriate connections during development.

The term SCI lesion refers to the disrupted spinal cord tissue resulting from mechanical trauma. The development of this lesion over time, often results in an expansion of the initial injury. This extension depends on the reaction to the initial injury of various cell types including astrocytes, microglia, hematogenous macrophages, fibroblasts, and pericytes,. This injury response in the CNS is characterized by glial and stromal scarring and deposition of inhibitory factors that serve as barriers to axonal regeneration.

Microglia are among the first CNS cell types to respond to injury by sensing adenosine triphosphate (ATP) released from damaged tissue. Within minutes they extend processes toward the lesion site, which fuse together in an attempt to contain the damaged area.[3] In response to injury microglia become activated, transitioning from a ramified to an amoeboid morphology,[4,5] and produce inflammatory cytokines that contribute to secondary injury and scarring responses.[6]

Myelin-associated inhibitors released from damaged oligodendrocytes, such as Nogo-A,[7] myelin-associated glycoprotein (MAG),[8,9] and oligodendrocyte-myelin glycoprotein (OMgp),[10] accumulate within the lesion site to inhibit

[1]Mayo Clinic College of Medicine, Mayo Clinic, Rochester, Minnesota.
[2]Mayo Graduate School, Mayo Clinic, Rochester, Minnesota.
Departments of [3]Neurology and [4]Orthopedic Surgery, Mayo Clinic, Rochester, Minnesota.
[5]Center for Regenerative Medicine, Mayo Clinic, Rochester, Minnesota.

axon regeneration. Macrophage recruitment and phagocytosis of myelin is delayed in the CNS,[11] and these macrophages are not able to efficiently process phagocytosed myelin, undergoing necrotic and apoptotic cell death.[12]

The glial scarring response refers to astrocytes taking on a reactive phenotype characterized by increased glial fibrillary acidic protein (GFAP) expression, hypertrophy, proliferation, and altered gene expression.[13] To a certain extent, reactive astrogliosis is beneficial in the restoration of the blood brain barrier and regulation of leukocyte trafficking into the CNS.[14] However, the reactive astrocytes forming this glial scar also produce chondroitin sulfate proteoglycans (CSPG) that impair axonal regeneration.[15–17]

Another important barrier to axonal regeneration after SCI is the stromal, or connective tissue, scar that forms at the injury site. This stromal scar is mainly the result of collagen production by fibroblasts and pericytes, which forms a physical barrier and serves as a framework for the deposition of axon growth inhibitory molecules such as semaphorin-3A (Sema3A), tenascin-C, and the CSPGs phosphocan and neuron-glial antigen 2 (NG2).[18–21] Release of profibrotic cytokines, such as transforming growth factor-β1 and -β2 (TGF-β1 and TGF-β2), by microglia and infiltrating macrophages is thought to drive this scarring process.[22–23]

Tissue engineering represents a promising approach for modulating the inhibitory environment of the SCI lesion site to facilitate recovery. Other investigators have used a variety of biomaterials in SCI as injectable, nonstructured delivery vehicles after partial lesions such as hemisection,[24–29] contusion, or compression injury.[30,31] These incomplete lesion models spare a degree of CNS tissue at the injury site, thus in these models it is difficult to differentiate between true regeneration and distal axonal sprouting or remodeling. The complete transection lesion followed by scaffold placement provides a model where regeneration can be studied functionally and anatomically and the local environment in and around the scaffold precisely controlled.

Control over the local injury environment is achieved through incorporation of various cell types or pharmacological agents within the scaffolds, and through the chemical and physical properties of the scaffold itself. Previous studies in our laboratory have evaluated various polymers and cell types for nervous system repair.[32–44] Schwann cells loaded into polymer scaffold channels have demonstrated an increased capacity for supporting axonal regeneration when compared with other cell types such as neural stem cells or mesenchymal stem cells.[37,42] We have shown that biodegradable polymer hydrogel scaffolds seeded with Schwann cells are able to bridge the growth inhibitory lesion site and support axon regeneration *in vivo*.[36,40]

We have also compared the mechanical properties and regeneration supporting potential of various polymers, including poly(lactic-co-glycolic acid) (PLGA), poly(caprolactone fumarate) (PCLF), a neutral oligo[(polyethylene glycol) fumarate] (OPF) hydrogel, and a positively charged oligo [(polyethylene glycol) fumarate] (OPF+) hydrogel and determined that scaffolds fabricated from OPF+ support the most axon regeneration and have similar compression and flexural moduli to rat spinal cord.[45] OPF+ has also been shown to support neurite outgrowth and myelination of dorsal root ganglia when cocultured with Schwann cells *in vitro*.[35]

However, even the amount of axonal regeneration achieved with OPF+ scaffolds loaded with Schwann cells is not sufficient for inducing any significant recovery of hind limb function after complete spinal cord transection.[45] Thus, further optimization of these Schwann cell-loaded OPF+ scaffolds is necessary; requiring an analysis of the CNS tissue response to implantation in the injured spinal cord, which has not been a previous focus of study.

Immediately after implantation, biomaterials have been shown to be coated with coagulation, complement, and adhesion factors from the blood.[46–48] These adsorbed proteins facilitate the adhesion and activation of immune cells, leading to a foreign body response characterized by an initial influx of polymorphonuclear leukocytes followed by a later accumulation of monocytes that differentiate into macrophages.[46–48] Macrophages produce profibrotic factors such as TGF-β and platelet-derived growth factor, which cause fibroblasts to produce and deposit collagen that encapsulates the biomaterial foreign body.[46,47] Although macrophages can drive this foreign body response, they have also been shown to play a crucial role in resolving inflammation and scavenging debris after SCI to provide a more permissive environment for axon regeneration.[49–53]

Interactions with the protein-coated biomaterial can induce a phenotypic switch in the macrophages to an M2-like state, in which they secrete anti-inflammatory cytokines such as interleukin-10 (IL-10).[21–23] Macrophage activation and adhesion has been shown to be more robust with hydrophilic polymers that are charged rather than uncharged, with the activated macrophages showing an anti-inflammatory cytokine profile.[54] Therefore, the presence of an implanted OPF+ polymer scaffold could dramatically change the pattern of lesion development after SCI. Furthermore, Schwann cells are known to play a crucial role in directing the repair process after peripheral nerve injury, and they may also contribute to the modification of the lesion site when implanted after SCI.[55,56]

In this study we characterized the CNS tissue response over time to OPF+ scaffold implantation with or without Schwann cells loaded into the scaffold channels. This approach allowed us to investigate whether the loaded Schwann cells change the course of lesion development. We also compared animals subjected to spinal cord transection with or without scaffold implantation to determine the effects of the polymer in modifying the lesion environment. The results of this study thus provide insight into the benefits of OPF+ scaffold implantation, the role of transplanted Schwann cells, and the remaining barriers to axonal regeneration present after scaffold implantation, allowing the identification of potential therapeutic targets.

Materials and Methods

Scaffold production

OPF+ scaffolds were synthesized and constructed according to previously published methods.[35,42,44,45,57–61] The characteristics of the 20% charged OPF+ hydrogel have been previously described as having a zeta potential of 3.7 ± 1.1 mV, conductivity of 0.15 ± 0.02 mS cm^{-1}, pH of 4.09 ± 0.08, and sol fraction of $3.78\% \pm 1.87\%$ in deionized water.[62] The compression and flexural moduli of scaffolds made from OPF+ (0.13 ± 0.03 MPa and 1.87 ± 1.03 MPa, respectively) have also been previously determined not to be significantly different from those of rat spinal cord tissue (0.19 ± 0.09 MPa and

0.74 ± 0.14 MPa, respectively).[45] Our unpublished data showed a weight loss of about 14% for OPF+ in PBS after 5 weeks. This slow degradation rate was attributed to a highly cross-linked network. This observation was in accordance with a low sol fraction, which is a measure of cross-linking density. Briefly, 1 g of OPF macromer was dissolved in deionized water containing 0.05% (w/w) photoinitiator (Irgacure 2959; Ciba Specialty Chemicals) and 0.3 g N-vinyl pyrrolidinone (NVP). The polymer was given a positive charge by co-polymerizing with 20% [2-(methacryloyloxy) ethyl]-trimethylammonium chloride (MAETAC). This OPF+ solution was then injected into a glass tube with seven evenly spaced wires inserted to form the scaffold channels. After cross-linking under UV light for 1 h, the polymer was swelled in PBS and cut into 2 mm length segments, resulting in scaffolds with 2.6 mm diameter and internal channels measuring 450 μm in diameter. These scaffolds were disinfected by immersion in 40%, 70%, and 100% ethanol for 30 min each, followed by four changes of PBS, then left in PBS for 24 h at 4°C.

Primary Schwann cell isolation and culture

Primary green fluorescent protein $(GFP)^+$ Schwann cells were isolated from the sciatic nerves of green rat (CZ-004 [SD TgN(act-EGFP)OsbCZ-004]) postnatal day 4 Sprague Dawley rat pups as previously described.[36,37,42,45,63] Pups were humanely euthanized by intraperitoneal injection of sodium pentobarbital (Sleepaway, Fort Dodge Animal Health). The sciatic nerves were surgically removed under aseptic conditions and the epineurium was dissected away. The nerves were cut into 1 mm sections and digested for 45 min with 0.25% trypsin-EDTA (Mediatech, Inc.) and 0.03% collagenase (Sigma) in Hank's balanced salt solution (Gibco). Cells were triturated; pelleted for 5 min at 300 rcf; and then resuspended in DMEM/F12 medium containing 10% fetal bovine serum, 100 U/mL penicillin/streptomycin (Gibco), 2 μM forskolin (Sigma), and 10 ng/mL recombinant human neuregulin-1-β1 extracellular domain (R&D Systems). Cells were plated on 35-mm laminin-coated dishes and incubated at 37°C in 5% CO_2 for 48 h.

Scaffold loading

Scaffolds were loaded with Matrigel containing Schwann cells or Matrigel alone as previously described.[36,37,42,45] Schwann cells were removed from culture dishes through incubation with trypsin-EDTA, and then resuspended at a density of 10^5 cells/μL in chilled Matrigel (BD Biosciences). A gel-loading pipette tip was used to load each of the seven channels of the scaffold with Matrigel containing Schwann cells or Matrigel alone under a microscope at 4°C. The Matrigel was then allowed to become a gel within the channels at 37°C for 3 min. The loaded scaffolds were incubated in DMEM/F12 medium containing 10% fetal bovine serum, 100 U/mL penicillin/streptomycin (Gibco), 2 μM forskolin (Sigma), and 10 ng/mL recombinant human neuregulin-1-β1 extracellular domain (R&D Systems) for 24 h at 37°C in 5% CO_2 before implantation into animals.

Animal experiments

All animal procedures were performed according to the guidelines of the Mayo Clinic Institutional Animal Care and Use Committee (IACUC). Animals were kept on a standard 12 h light-dark cycle with access to food and water *ad libitum* in conventional housing in accordance with National Institutes of Health (NIH) and U. S. Department of Agriculture guidelines. A total of 56 adult female Sprague Dawley rats (Harlan Laboratories) weighing approximately 250 g were used in this study. Animal numbers per group were as follows: OPF + scaffolds with Matrigel containing Schwann cells week 1($N=4$), week 2 ($N=5$), week 3 ($N=4$), week 4 ($N=5$), and week 8 ($N=5$); OPF + scaffolds with Matrigel only week 1($N=3$), week 2 ($N=4$), week 3 ($N=5$), week 4 ($N=5$), and week 8 ($N=5$); and transection only without scaffold implantation week 4 ($N=11$).Bladders were expressed twice daily after surgery and animals were given antibiotics and analgesics as necessary. All rats were cared for under the advisement of veterinarians with experience in handling rats after SCI.

Spinal cord transection and scaffold implantation

Animals received acetaminophen (Mapap) in their drinking water (1:15) for 48 h before surgery. Animal weight was recorded. Female Sprague Dawley rats weighing approximately 250 g were anesthetized by intraperitoneal injection of a ketamine (Fort Dodge Animal Health) and xylazine (Lloyd Laboratories) mixture, 80 and 5 mg/kg, respectively. The animal's eyes were protected from drying out during surgery with Puralube Vet Ointment (Pharmaderm). After the animals were anesthetized, each received Buprenex (0.05 mg/kg; Reckitt Benckiser Pharmaceuticals, Inc.) intramuscularly, Baytril (65 mg/kg; Bayer Corporation) intraperitoneally, and five mL of lactated Ringer's solution (Baxter Healthcare Corporation) subcutaneously. Hair was clipped on the back of the spine with an electric hair clipper. The site of incision was scrubbed and disinfected using povidone-iodine scrub swabsticks (Professional Disposables, Inc.). Animals were placed on a heating pad and temperature was constantly maintained at 37°C during surgery.

Animals were randomly designated to each of eleven experimental groups: OPF+ scaffolds with Matrigel containing Schwann cells (week 1, week 2, week 3, week 4, and week 8 time points), OPF+ scaffolds with Matrigel only (week 1, week 2, week 3, week 4, and week 8 time points), and transection only without scaffold implantation (week 4 time point). A Zeiss F170 microsurgical microscope (Oberkochen) was used throughout the surgery. A two cm incision was made on the dorsal aspect of spine over the T_9-T_{10} vertebral level and sharply dissected to the spinous processes. Blunt and sharp dissection was used to elevate the paraspinous musculature exposing the lamina. A laminectomy was performed at the T_9-T_{10} vertebral level exposing the spinal cord. The spinal cord was completely transected using a No. 11 scalpel (BD Medical). Complete transection was verified with a hooked probe. After transection, the two cut ends of the spinal cord retracted to form a two mm gap at the T_9-T_{10} vertebral level. Prepared scaffolds were implanted between the free ends of the spinal cord, with the scaffold channels oriented parallel to the length of the spinal cord. The wound was closed in two separate muscle and skin layers with absorbable 3.0 vicryl sutures using simple interrupted stitches. After spinal cord transection all animals were kept at 37°C on heating pads

for the next 24 h. Animals were monitored regularly until fully conscious.

Postsurgical care

Animals were kept in low-walled cages to allow easy access to food and water. Animals received acetaminophen (Mapap; Major Pharmaceutiacals) in their drinking water (1:15) for 48 h before surgery and for 7 days after surgery. Buprenex (0.05 mg/kg; Reckitt Benckiser Pharmaceuticals, Inc.) intramuscularly and Baytril (65 mg/kg; Bayer Corporation) intraperitoneally were administered twice daily for 5 and 7 days postsurgery, respectively, and then as needed for pain or bladder infection thereafter. Five mL of lactated Ringer's solution (Baxter Healthcare Corporation) were also given subcutaneously twice daily for 5 days postsurgery. Bladders were manually expressed twice daily for the duration of the experiment, and the animals' urine was monitored for signs of bladder infection.

Tissue preparation and sectioning

At the conclusion of the experiment, animals were humanely euthanized with an intraperitoneal injection of 0.4 mL sodium pentobarbital (40 mg/kg) (Fort Dodge Animal Health) and transcardially perfused through the aorta with 60 mL of PBS followed by 60 mL of 4% paraformaldehyde. The vertebral column with spinal cord was removed *en block* and postfixed overnight in 4% paraformaldehyde at 4°C. Five mm of spinal cord containing the lesion site and implanted scaffold was then dissected from the vertebral column and then processed for paraffin embedding. The spinal cord segments were cut longitudinally into 10 μm sections on a Reichert-Jung Biocut microtome (Leica) and collected on numbered slides.

Masson trichrome staining

Slides with longitudinal sections were selected from the middle of the spinal cord for staining with the Masson trichrome kit (Thermo Scientific). Sections were first deparaffinized with xylene, then rehydrated with graded ethanol, and rinsed with distilled water. Sections were then placed in Bouin's Fluid at 56°C for 1 h, Working Weigert's Iron Hematoxylin Stain for 10 min, Biebrich scarlet-acid fuchsin solution for 5 min, phosphotungstic-phosphomolybdic acid solution for 5 min, Aniline blue stain solution for 5 min, and 1% acetic acid solution for 1 min as per kit instructions. Stained sections were then dehydrated in two changes of 100% ethanol, cleared with three changes of xylene, and mounted with Cytoseal 60 mounting medium (Richard-Allan Scientific). Images were acquired using the Neurolucida software (MBF Bioscience) on a modified Zeiss Axioimager A-1 microscope (Zeiss) equipped with a motorized specimen stage for automated sampling (Ludl Electronics) and a QICAM 12-bit Color Fast 1394 camera (QImaging).

Immunohistochemistry

Slides with longitudinal sections were selected from the middle of the spinal cord, near the Masson trichrome-stained slides, for immunohistochemistry. Sections were first deparaffinized with xylene, then rehydrated with graded ethanol, and rinsed with distilled water. Heat mediated antigen retrieval was performed by incubating the sections in 1 mM EDTA in PBS for 30 min in a rice steamer. Sections were allowed to cool to room temperature and then washed with 0.1% Triton X-100 in PBS before blocking with 10% normal donkey serum (NDS) in PBS for 30 min to prevent nonspecific antibody binding. Sections were incubated overnight at 4°C in primary antibody diluted in 5% NDS with 0.3% Triton X-100 in PBS. Sections were then washed with 0.1% Triton X-100 in PBS before incubating for one hr in secondary antibody diluted in 5% NDS with 0.3% Triton X-100 in PBS. After washing with 0.1% Triton X-100 in PBS, sections were mounted with SlowFade Gold Antifade Reagent with DAPI (Molecular Probes). Images were acquired using the Neurolucida software (MBF Bioscience) on a modified Zeiss Axioimager A-1 microscope (Zeiss) equipped with a motorized specimen stage for automated sampling (Ludl Electronics) and a QICAM 12-bit Color Fast 1394 camera (QImaging). Confocal images were acquired using a LSM 780 confocal microscope (Zeiss) with a C-Apochromat 40×/1.20 water immersion objective with 2.6 zoom.

The primary antibodies and their dilutions used in this study were as follows: Rabbit anti-green fluorescent protein (GFP) polyclonal antibody (MBL International Corporation; JM-3999-100, 1:400), Rabbit anti-GFAP polyclonal antibody (Dako; Z0334, 1:1600), Mouse anti-neurofilament (NF) monoclonal antibody (Dako; clone 2F11, 1:100), Mouse anti-chondroitin sulfate monoclonal antibody (Sigma-Aldrich; clone CS-56, 1:100), Rabbit anti- myelin basic protein (MBP) polyclonal antibody (Abcam; ab40390, 1:800), Goat anti-MBP polyclonal antibody (Santa Cruz Biotechnology; sc-13914, 1:400), Rabbit anti-ionized calcium binding adapter molecule 1 (Iba1) polyclonal antibody (Wako; 019-19741, 1:800), Rabbit anti- CD86 monoclonal antibody (Abcam; ab53004, 1:400), and Goat anti-macrophage mannose receptor (MMR)/CD206 polyclonal antibody (R&D Systems; AF2535, 1:50).

The secondary antibodies and their dilutions used in this study were as follows: Donkey anti-goat FITC-conjugated antibody (Millipore; AP180F, 1:100), Donkey anti-rabbit Cy3-conjugated antibody (Millipore; AP182C, 1:200), Donkey anti-rabbit FITC conjugated antibody (Millipore; AP182F, 1:100), and Donkey anti-mouse Cy3-conjugated antibody (Millipore; AP192C, 1:200).

Analysis of stain distance from tissue-scaffold interface

The distances that the collagen and fibrinoid scar extended rostrally or caudally from the tissue-scaffold interface were measured by overlaying a grid with 500 μm divisions on the Masson trichrome-stained tissue sections. Wherever this grid intersected with the tissue-scaffold interface, three to five measurement lines (depending on the width of the tissue-scaffold interface) were drawn parallel to the length of the spinal cord to the furthest extent of the fibrinoid or collagen scar along these lines. The distances of NF^+ axons, perineuronal net CSPG, and $GFAP^+$ astrocytes away from the tissue-scaffold interface were similarly measured by overlaying the grid on the respectively stained tissue sections. Measurements were made from the tissue-scaffold interface to the first NF^+ axons, perineuronal net CSPG, or $GFAP^+$ astrocytes that displayed the normal tissue architecture of uninjured spinal cord (Supplementary Fig.

S1A–C; Supplementary Data are available online at www.liebertpub.com/tea). Measurements of each stain from the rostral and caudal tissues were averaged for each animal. The standard deviation of these four to six distance measurements were under 37% of their averaged value for collagen scar, under 30% for fibrinoid scar, under 25% for GFAP, under 19% for NF, and under 20% for CSPG. See Figure 1 for schematic diagram of analysis.

Analysis of stromal scar and cyst areas

The areas of the collagen and fibrinoid scars were measured by drawing a contour around the stromal lesion in the Masson trichrome-stained tissue sections. The stromal lesion was defined as the area of visibly disrupted tissue on Masson trichrome-stained sections containing collagen scarring, fibrinoid scarring, or cysts. For scaffold-implanted animals, this contour consisted of separate rostral and caudal lesion sites that extended from the tissue-scaffold interface and were summed together, while in transection only animals the contour consisted of the entire continuous lesion. A grid with 100 μm divisions was overlaid on the tissue, and markers for collagen or fibrinoid scar were placed at each grid intersection within the stromal lesion contour. The area of collagen or fibrinoid scar within the stromal lesion contour was then calculated using the Cavalieri probe in the Stereo

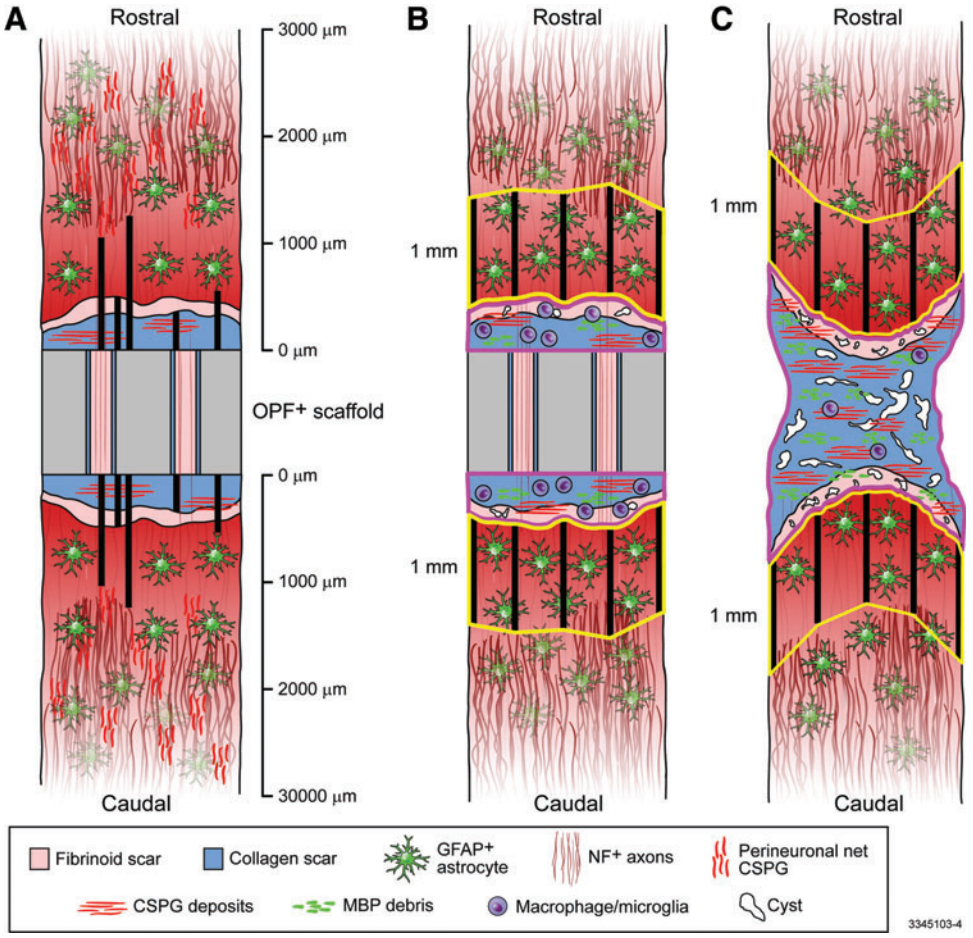

FIG. 1. Diagrams describing the methods of analysis. **(A)**: Distance measurements (*thick black lines*) were taken from the tissue-scaffold interface to the furthest extent of the collagen and fibrinoid scars, and from the tissue-scaffold interface to the nearest $GFAP^+$ astrocytes, NF^+ axons, and perineural net CSPG (CSPG deposits within the lesion site were ignored for this analysis). These measurements were taken on both the rostral and caudal sides of the OPF+ scaffold, wherever a grid with 500 μm divisions intersected with the tissue-scaffold interface, and were averaged. Collagen scar areas, fibrinoid scar areas, cyst areas, CSPG deposit areas, MBP debris areas, $Iba1^+$ cell counts, $CD86^+$ cell counts, and $CD206^+$ cell counts were measured within contours (*pink outlines*) drawn around the stromal scar rostral and caudal to the OPF+ scaffold and then summed in polymer-implanted animals **(B)**, these measurements were taken within a contour (*pink outline*) drawn around the continuous stromal scar in animals with transection only **(C)**. The $GFAP^+$ proportional area was measured within contours (*yellow outlines*) drawn one mm rostral and caudal to the stromal lesion. These contours were drawn by extending one mm measurement lines (*thick black lines* in **B** and **C**) out from the distal boarder of the stromal lesion and connecting the distal end points of these lines. $GFAP^+$ proportional area was then measured in the area between these end points and the distal boarder of the stromal lesion. This measurement was taken on both the rostral and caudal sides of the lesion, which were then averaged. CSPG, chondroitin sulfate proteoglycan; MBP, myelin basic protein. Color images available online at www.liebertpub.com/tea

Investigator software (MBF Bioscience). Cyst areas were identified as fluid filled cavities and measured by drawing contours around them in the Neurolucida software (MBF Bioscience). See Figure 1 for schematic diagram of analysis.

Analysis of GFAP$^+$ proportional area

The proportional area positive for GFAP was measured in a region of interest (ROI) within one mm rostral or caudal to the stromal lesion. This ROI was obtained by first using the Masson trichrome-stained tissue as a guide to draw a contour around the stromal lesion on the GFAP-stained tissue. Five measurement lines, evenly spaced along the distal portion of the stromal lesion contour, were then drawn parallel to the length of the spinal cord to extend one mm out rostrally or caudally. The ROI contour was then drawn by connecting the distal points of these measurement lines and then enclosing the tissue from these points to the stromal lesion contour. Automatic object detection was then used in the Neurolucida software (MBF Bioscience) to draw contours around the GFAP$^+$ astrocytes within this ROI contour. The sum of the GFAP$^+$ contour areas was then divided by the total area of the ROI contour to obtain the GFAP$^+$ proportional area. Measurements from the rostral and caudal ROIs were averaged for each animal. See Figure 1 for schematic diagram of analysis.

Analysis of Iba1$^+$, CD86$^+$, and CD206$^+$ cell counts

Iba1$^+$, CD86$^+$, and CD206$^+$ cells were counted within the stromal lesion by first using the Masson trichrome-stained tissue as a guide to draw a contour around the stromal lesion on the respectively stained tissue. For scaffold-implanted animals, this contour consisted of separate rostral and caudal lesion sites that extended from the tissue-scaffold interface and were summed together, while in transection only animals the contour consisted of the entire continuous lesion. Iba1$^+$, CD86$^+$, and CD206$^+$ cells were counted in the Neurolucida software (MBF Bioscience) by placing a marker on cells that were within the stromal lesion contour, positive for the respective stain, and contained a DAPI$^+$ nucleus. Iba1$^+$ cells with an amoeboid morphology indicative of an activated state[64] (Supplementary Fig. S2B, C) were counted separately from Iba1$^+$ cells without an amoeboid morphology. See Figure 1 for schematic diagram of analysis.

Analysis of GFP, CSPG, and MBP area

GFP, CSPG, and MBP areas were measured within the stromal lesion by first using the Masson trichrome-stained tissue as a guide to draw a contour around the stromal lesion on the respectively stained tissue. For scaffold-implanted animals, this contour consisted of separate rostral and caudal lesion sites that extended from the tissue-scaffold interface and were summed together, while in transection only animals the contour consisted of the entire continuous lesion. Automatic object detection was then used in the Neurolucida software (MBF Bioscience) to draw contours around the GFP$^+$ Schwann cells, CSPG deposits, or MBP$^+$ myelin debris within this stromal lesion contour. The sum of the contour areas outlined within the lesion site with automatic object detection for each stain was then used for analysis. See Figure 1 for schematic diagram of analysis.

Statistical analysis

Where possible, analyses were done by observers blinded to animal group. When comparing animals with and without scaffolds blinding was not possible. The GFP area within the rostral and caudal stromal lesion of animals with scaffolds containing Schwann cells was analyzed over time by two-way analysis of variance (ANOVA). The change in distance from the tissue-scaffold interface over time of the collagen scar, fibrinoid scar, GFAP$^+$ astrocytes, NF$^+$ axons, and perineuronal net CSPG was compared between animals with scaffolds containing Schwann cells and animals with scaffolds containing Matrigel only by two-way ANOVA. The change in area of the collagen scar and fibrinoid scar was also compared over time between animals with scaffolds containing Schwann cells and animals with scaffolds containing Matrigel only by two-way ANOVA. The fibrinoid scar area, collagen scar area, cyst area, GFAP$^+$ proportional area, CSPG area, and MBP area at 4 weeks postinjury were compared by Student's unpaired t tests between the animals with scaffolds containing Schwann cells and animals with scaffolds containing Matrigel only, and also between the combined polymer-implanted animals (scaffolds with and without Schwann cells) and the animals with transection only. Cell counts of Iba1$^+$ cells with and without amoeboid morphology, CD86$^+$ cells, and CD206$^+$ cells at 4 weeks postinjury were analyzed among the animals with scaffolds containing Schwann cells, animals with scaffolds containing Matrigel only, and animals with transection only by one-way ANOVA with *post hoc* analysis using Tukey's multiple comparison test. Statistical analyses were performed using GraphPad Prism 6 (GraphPad Software, Inc.) and JMP 10 (SAS Institute, Inc.) software. All data are presented as mean $\pm$ standard deviation. Values of $p < 0.05$ were considered statistically significant.

Results

Fate of GFP$^+$ Schwann cells

To follow the fate of the transplanted donor GFP$^+$ Schwann cells, longitudinal tissue sections were immunostained for GFP. A two-way ANOVA was conducted on the GFP area within the lesion site, with time postimplantation (1, 2, or 3 weeks) and lesion side (rostral or caudal) as factors (Supplementary Table S1). Many Schwann cells were observed within the scaffold channels at 1 and 2 weeks postimplantation. Schwann cells also migrated into the rostral and caudal lesion over these first 2 weeks, with more cells accumulating in the caudal lesion ($p < 0.05$ for main effect of lesion side) (Fig. 2A, B). The GFP$^+$ Schwann cells retained a spindle-shaped morphology (Fig. 2E). However, at 3 weeks postimplantation there was a significant reduction in GFP Schwann cells observed in both the scaffold channels and the lesion ($p < 0.05$ for main effect of time postimplantation) (Fig. 2C, D). GFP$^+$ donor Schwann cells were not observed at 4 or 8 weeks postimplantation.

Time course evaluation of CNS tissue reaction to scaffold implantation

In concordance with previous results from our laboratory, no recovery of hind limb function was observed in scaffold-implanted animals.[45] The CNS tissue response to scaffold implantation with or without donor Schwann cells was

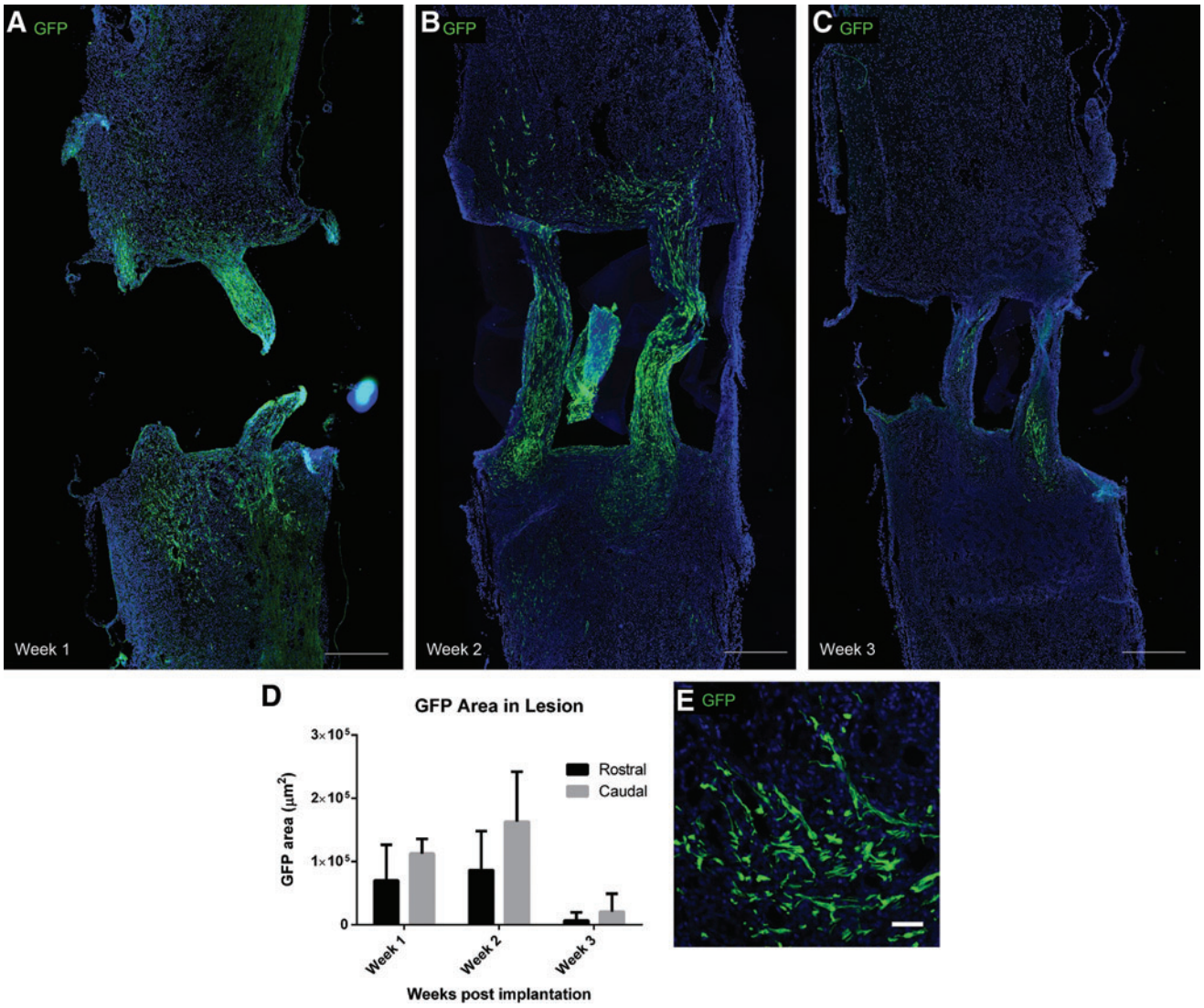

FIG. 2. Transplanted GFP$^+$ Schwann cell (*green*) migration from OPF+ scaffold channels into the rostral and caudal SCI lesion at 1 week **(A)**, 2 weeks **(B)**, and 3 weeks **(C)** postpolymer scaffold implantation (Scale bars: 500 μm). **(D)**: Quantified GFP area within the rostral and caudal lesions. $p < 0.05$ for main effects of time postimplantation and lesion side. **(E)**: High power image of GFP$^+$ Schwann cells displaying spindle-shaped morphology (Scale bar: 50 μm). SCI, spinal cord injury; GFP, green fluorescent protein. Color images available online at www.liebertpub.com/tea

compared histologically by evaluating stromal scarring, NF$^+$ axons, perineuronal net CSPG, and GFAP$^+$ astrocytes (Supplementary Fig. S1A–C). A two-way ANOVA was conducted on the distance of each stain (collagen scar, fibrinoid scar, GFAP$^+$ astrocytes, NF$^+$ axons, or perineuronal net CSPG) from the tissue-scaffold interface, with time postimplantation (1, 2, 3, 4, or 8 weeks) and group (scaffolds with Schwann cells or scaffolds with Matrigel only) as factors (Supplementary Table S1). A two-way ANOVA was also conducted on the collagen scar area and fibrinoid scar area, again with time postimplantation and group as factors (Supplementary Table S1).

Masson trichrome staining showed an initially large fibrinoid scar area extending from the tissue-scaffold interface that receded over 8 weeks ($p < 0.05$ for main effect of time postimplantation, fibrinoid scar area and distance). This fibrinoid scar was replaced over time with a collagen barrier forming at the tissue-scaffold interface, resulting in collagen completely filling the scaffold channels by 8 weeks postimplantation ($p < 0.05$ for main effect of time postimplantation, collagen scar area, and distance) (Fig. 3A–E and Supplementary Fig. S3D). There was no difference in the development of this stromal scar between the Schwann cell-containing or Matrigel-only scaffold-implanted groups ($p > 0.05$ for main effect of group, fibrinoid and collagen scar area and distance).

The influence of stromal scar development on the infiltration of normal CNS tissue was also examined by measuring the distance of the boundary of each stain from the tissue-scaffold interface. The advancement of GFAP$^+$ astrocytes matched the recession of the fibrinoid scar toward the tissue-scaffold interface over time ($p < 0.05$ for main effect of time postimplantation, GFAP$^+$ astrocyte distance) (Supplementary Fig. S3A–D). While some NF$^+$ axons were

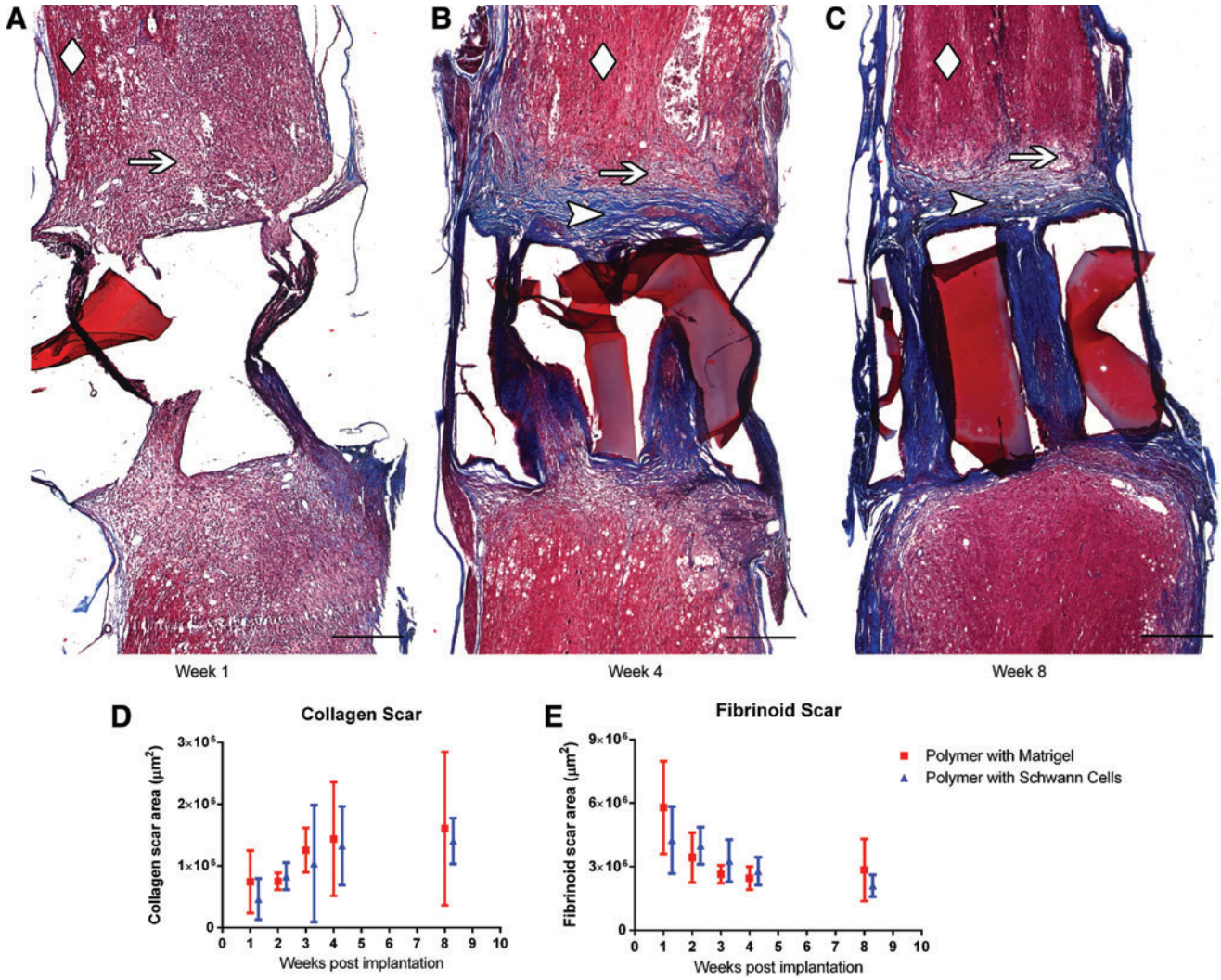

FIG. 3. Masson trichrome staining showing stromal scar development at 1 week **(A)**, 4 weeks **(B)**, and 8 weeks **(C)** postpolymer scaffold implantation (Scale bars: 500 µm). Uninjured spinal cord tissue is designated with a *diamond*, fibrinoid scar with an *arrow*, and collagen scar with an *arrowhead*. The fragments of OPF+ scaffold material were present in all sections. The mounting process floated them to different positions but this did not interfere with measurements. Quantification of collagen scar area **(D)** and fibrinoid scar area **(E)** over time in animals implanted with scaffolds containing Schwann cells or Matrigel only. $p < 0.05$ for main effect of time postimplantation for collagen and fibrinoid scar areas. Color images available online at www.liebertpub.com/tea

able to cross the stromal scar and enter the scaffold channels, the bulk of NF^+ axons (Supplementary Fig. S4A–C) and perineuronal net CSPG (Supplementary Fig. S4D–F) remained at a constant distance away from the tissue-scaffold interface ($p > 0.05$ for main effect of time postimplantation, NF^+ axons and perineuronal net CSPG distances) (Supplementary Fig. S3D).

No difference was observed between the Schwann cell-containing or Matrigel-only scaffold-implanted groups in the distance from the tissue- scaffold interface of NF^+ axons, perineuronal net CSPG, or $GFAP^+$ astrocytes ($p > 0.05$ for main effect of group, NF^+ axons, perineuronal net CSPG, and $GFAP^+$ astrocytes distance). With the exception of some individual NF^+ axons, none of these normal CNS tissue components were observed to advance beyond the stromal scar. The trends of fibrinoid scar recession, collagen scar accumulation, and $GFAP^+$ astrocyte advancement over time appeared to stabilize by 4 weeks postimplantation (Supplementary Fig. S3D).

Influence of scaffold implantation on lesion environment at 4 weeks postinjury

The influence of the polymer scaffold on the lesion environment was evaluated by comparing the combined scaffold-implanted animals (with and without donor Schwann cells) with animals receiving a transection injury without scaffold implantation. This evaluation was performed at 4 weeks postinjury, since the scarring process had stabilized at this time, as shown by the time course data described above and in Supplementary Figure S3D.

Stromal scar. Polymer-implanted animals had a significantly reduced collagen scar area compared to those with

transection only (Fig. 4A–C), while there was no significant difference in fibrinoid scar area ($2.6\times10^6\pm0.6\times10^6$ μm^2 vs. $3.0\times10^6\pm0.9\times10^6$ μm^2, respectively, $p>0.05$). Cyst area was also significantly reduced in the polymer-implanted animals (Fig. 4D). There was no significant difference between polymer-implanted animals with or without Schwann cells in collagen scar area ($1.3\times10^6\pm0.6\times10^6$ μm^2 vs. $1.4\times10^6\pm0.9\times10^6$ μm^2, respectively, $p>0.05$), fibrinoid scar area ($2.8\times10^6\pm0.7\times10^6$ μm^2 vs. $2.5\times10^6\pm0.6\times10^6$ μm^2, respectively, $p>0.05$), or cyst area ($1.2\times10^5\pm0.9\times10^5$ μm^2 vs. $1\times10^5\pm1\times10^5$ μm^2, respectively, $p>0.05$).

GFAP$^+$ astrocytes. GFAP$^+$ astrocytes were analyzed within one mm rostral or caudal to the stromal lesion (as shown in Fig. 1). Astrocytes in animals with transections only had a more reactive phenotype, with GFAP expression extending into the distal processes of the cells, in contrast to the GFAP staining in polymer-implanted animals, which was limited to the cell body and proximal processes (Fig. 5A, B). The proportional GFAP$^+$ area measured within one mm rostral and caudal to the lesion was significantly reduced in the polymer-implanted animals (Fig. 5F). No significant difference was observed in proportional GFAP$^+$ area between polymer-implanted animals with or without Schwann cells (0.10 ± 0.04 vs. 0.11 ± 0.04, respectively, $p>0.05$).

Iba1$^+$ macrophages/microglia. Activated, Iba1-stained macrophages/microglia with amoeboid morphology[64] were quantified within the lesion site. Resting Iba1$^+$ microglia with a ramified morphology were mainly found in the uninjured spinal cord away from the lesion site (Supplementary Fig. S2A). Amoeboid Iba1$^+$ cells were most abundant in the lesions of animals with scaffolds containing Schwann cells, followed by those with Matrigel-only scaffolds, and were least abundant in animals with transection only (Fig. 5C–E, G). The number of Iba1$^+$ cells without an amoeboid phenotype was not different among the three groups ($p>0.05$), and these cells were a minority of the total Iba1$^+$ cells ($12\%\pm7\%$, $21\%\pm4\%$, and $40\%\pm10\%$ for animals with Schwann cell-loaded scaffolds, animals with Matrigel-only scaffolds, and animals with transection only, respectively).

Amoeboid Iba1$^+$ cells were often found in close association with MBP deposits, and Iba1$^+$ cells were observed containing intracellular MBP (Supplementary Fig. S2B). Cells containing MBP had less intense Iba1 expression on their plasma membrane than cells that did not contain MBP (Supplementary Fig. S2B–C). MBP deposits that were not contained by Iba1$^+$ cells were also observed in the lesion site (Supplementary Fig. S2D).

Macrophage/microglial phenotype. We attempted to classify the macrophages/microglia within the lesion site by staining for two cell surface markers of the proinflammatory M1 and anti-inflammatory M2 phenotype, CD86 and CD206, respectively. No significant difference was found in the number of CD86$^+$ cells within the lesions of polymer-implanted animals with Schwann cells, polymer-implanted animals without Schwann cells, or animals with transection

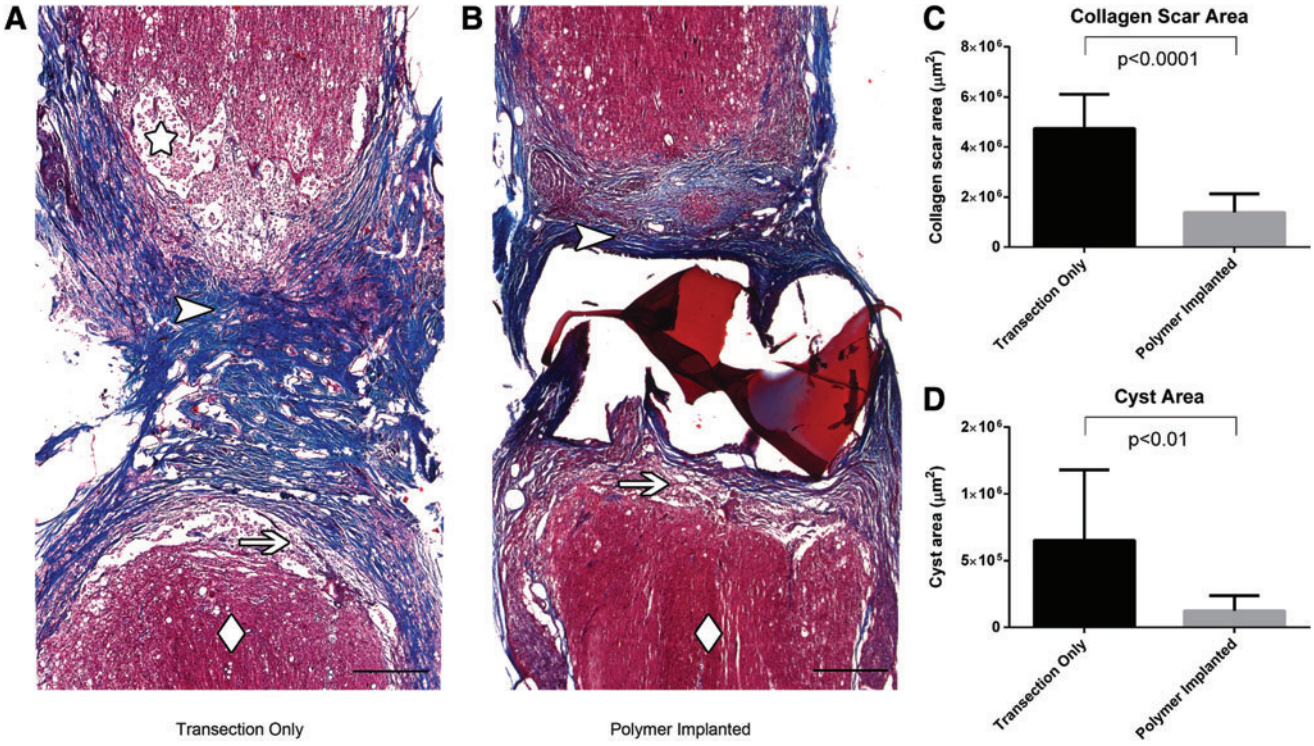

FIG. 4. Masson trichrome staining comparing stromal scarring in animals with transection only **(A)** versus implanted polymer scaffolds **(B)** at 4 weeks postinjury (Scale bars: 500 μm). Uninjured spinal cord tissue is designated with a diamond, fibrinoid scar with an *arrow*, collagen scar with an *arrowhead*, and cyst with a *star*. Note that the normal spinal cord tissue approaches the boundary of the lesion more closely and there are less cystic cavities in the scaffold-implanted animals. Quantification of collagen scar area **(C)** and cyst area **(D)** at 4 weeks postinjury in animals with transection only and implanted polymer scaffolds. Color images available online at www.liebertpub.com/tea

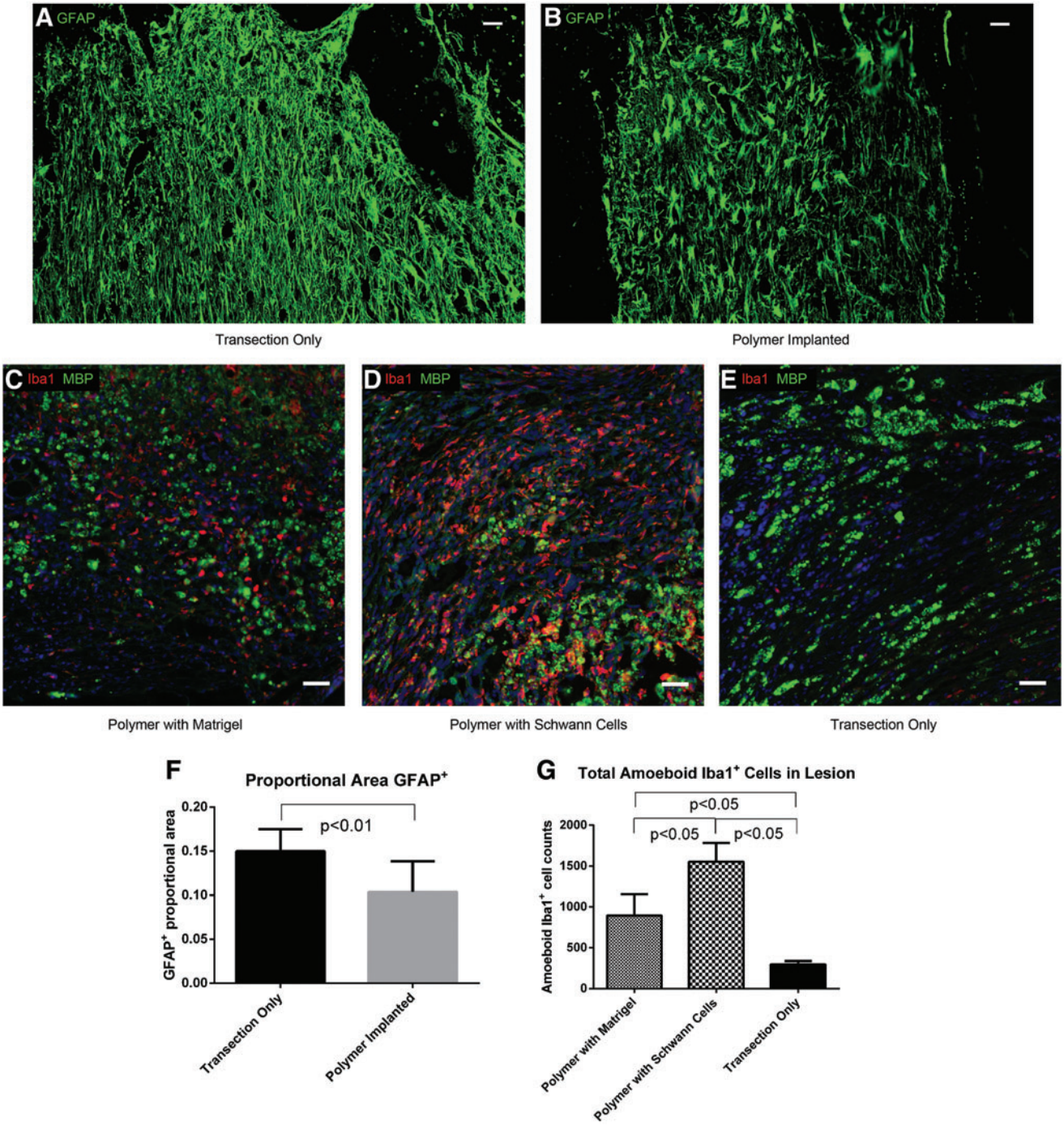

FIG. 5. GFAP$^+$ astrocytes and Iba1$^+$ macrophage/microglia at 4 weeks postinjury. GFAP expression extends into the distal processes of astrocytes in animals with transection only **(A)**, but is restricted to the cell bodies and proximal processes of astrocytes in animals with implanted polymer scaffolds **(B)** (Scale bars: 50 μm). Iba1 (*red*) and MBP (*green*) staining within the lesions of animals with implanted polymer scaffolds containing Matrigel only **(C)**, with implanted polymer scaffolds containing Schwann cells **(D)**, and with transection only **(E)** (Scale bars: 50 μm). **(F)**: Quantification of the proportion of the area within one mm of the stromal scar that is GFAP$^+$ in animals with transection only and with implanted polymer scaffolds. **(G)**: Amoeboid Iba1$^+$ cell counts within the lesions of animals with implanted polymer scaffolds containing Matrigel only, with implanted polymer scaffolds containing Schwann cells, and with transection only. GFAP, glial fibrillary acidic protein. Color images available online at www.liebertpub.com/tea

only (Fig. 6A–D). There was a trend for an increased number of CD206$^+$ cells within the lesions of animals with transection only; however this increase was only statistically significant when compared to the polymer-implanted animals without Schwann cells (Fig. 6A–C, E).

The total number of cells labeled with either CD86 or CD206 was also compared to the number of amoeboid Iba1$^+$ cells within the lesion site. Interestingly, the ratio of CD86$^+$ and CD206$^+$ cells combined to amoeboid Iba1$^+$ cells was 2 ± 1 in the transection only animals, while only 0.3 ± 0.2

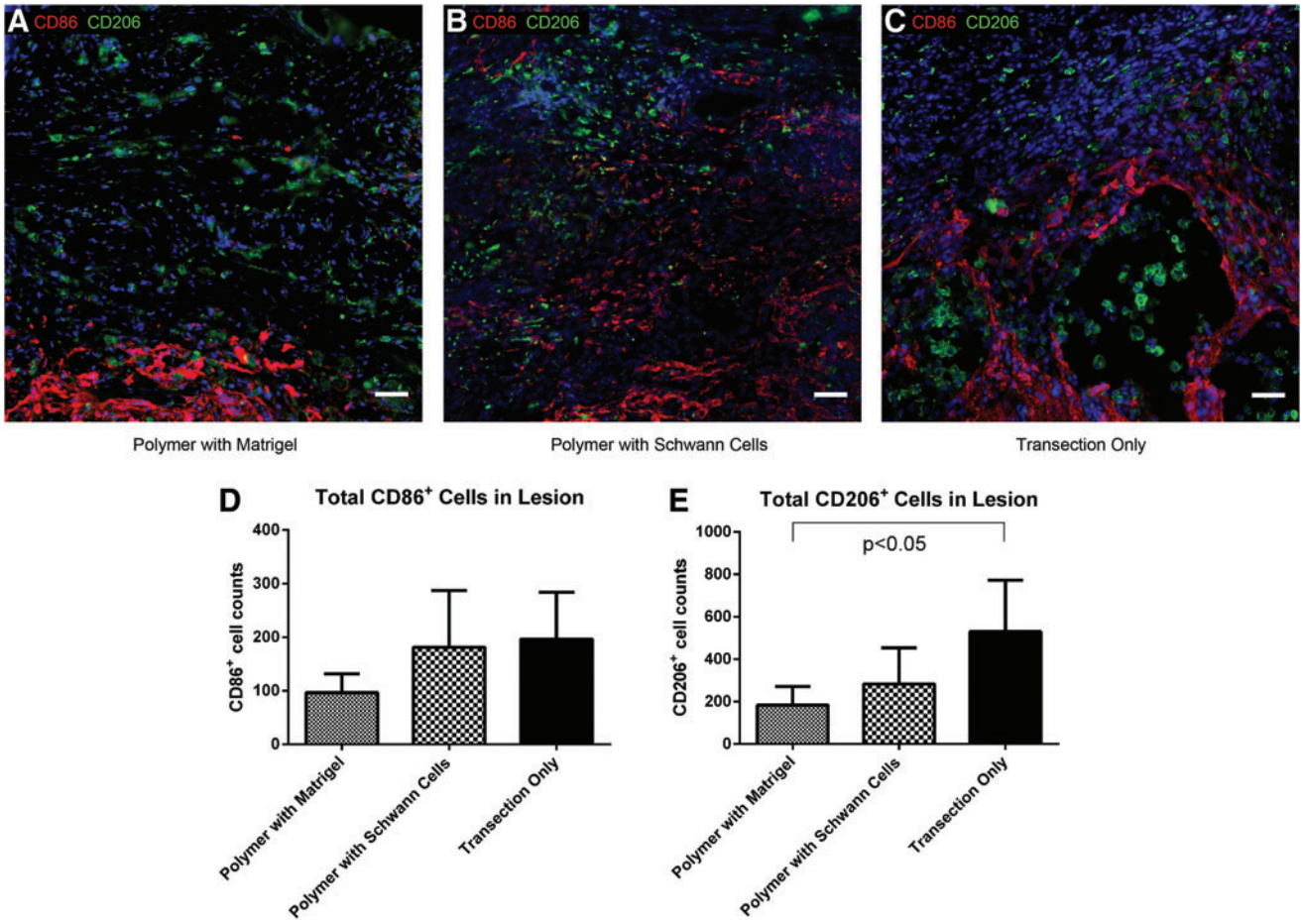

FIG. 6. CD86 (*red*) and CD206 (*green*) staining at 4 weeks postinjury within the lesions of animals with implanted polymer scaffolds containing Matrigel only **(A)**, with implanted polymer scaffolds containing Schwann cells **(B)**, and with transection only **(C)** (Scale bars: 50 μm). $CD86^+$ **(D)** and $CD206^+$ **(E)** cell counts within the lesions of animals with implanted polymer scaffolds containing Matrigel only, with implanted polymer scaffolds containing Schwann cells, and with transection only. Color images available online at www.liebertpub.com/tea

and 0.3 ± 0.2 in the polymer-implanted animals with or without Schwann cells, respectively. This discrepancy suggests that most of the macrophages/microglia within the lesions of the polymer-implanted animals were polarized to an unknown phenotype that could not be identified through staining with CD86 or CD206, while these markers were sufficient to identify most macrophages/microglia in animals with transection only. The sum of the cells labeled with CD86 and CD206 was higher than the number of amoeboid $Iba1^+$ cells in the transection only animals because only cells with amoeboid morphology were included for Iba1 counting, while all cells were included in the CD86 and CD206 counts regardless of morphology.

CSPG and MBP. The amounts of two major molecular barriers to axonal regeneration, CSPG and myelin debris (analyzed through MBP staining), were compared in the polymer implanted versus transection only animals. CSPG area was reduced in the lesions of polymer-implanted animals compared with those with transection only (Fig. 7A–C). The CSPG deposits in transection only animals were found to extend across the lesion site perpendicular to the direction of axon growth, in contrast to the punctate deposits found in the lesions of polymer-implanted animals (Supplementary Fig. S5A, B). MBP area was also reduced in the lesions of polymer-implanted animals compared with those with transection only (Fig. 7D–F, refer to Supplementary Fig. S5C, D for high power images). No significant difference was found between polymer-implanted animals with or without Schwann cells in CSPG area ($1.0 \times 10^5 \pm 0.6 \times 10^5$ μm^2 vs. $2 \times 10^5 \pm 1 \times 10^5$ μm^2, respectively, $p > 0.05$) or MBP area ($1.7 \times 10^5 \pm 0.7 \times 10^5$ μm^2 vs. $2 \times 10^5 \pm 1 \times 10^5$ μm^2, respectively, $p > 0.05$).

Discussion

In this study we have shown a distinctive reaction over time to OPF+ polymer scaffolds implanted into the SCI lesion site. The ends of the scaffold were initially capped with a fibrinoid scar at 1 and 2 weeks postimplantation, which receded over time. $GFAP^+$ astrocytes advanced toward the tissue-scaffold interface as the fibrinoid scar receded. There was a fibrotic response to the scaffold, resulting in a collagen barrier forming at the tissue-scaffold interface, with collagen completely filling the scaffold channels by 8 weeks postimplantation. This collagen deposition was likely a result of

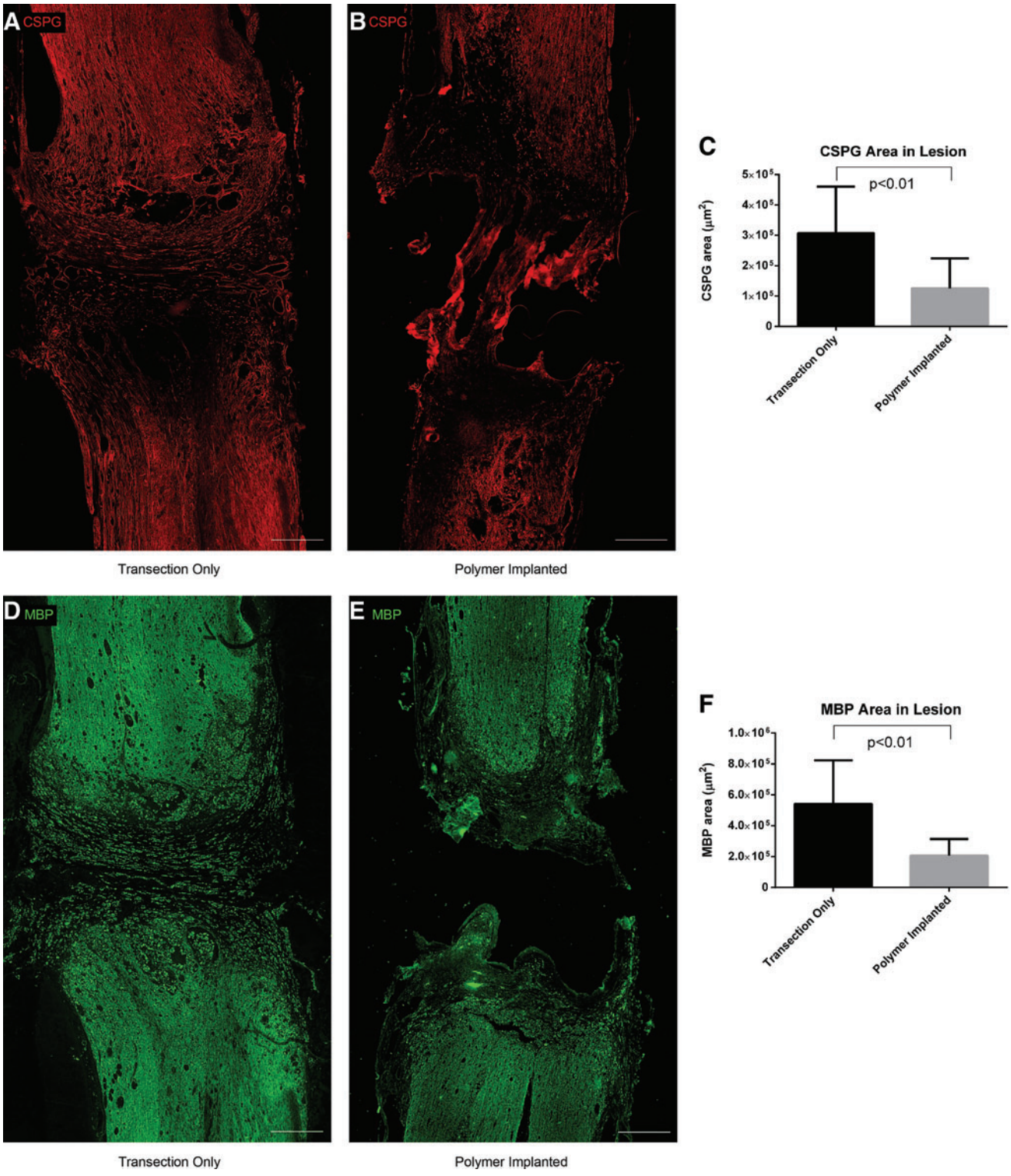

FIG. 7. CSPG deposits and MBP debris at 4 weeks postinjury. CSPG deposits extend across the lesion site in animals with transection only **(A)**, in contrast to the punctate deposits in animals with implanted polymer scaffolds **(B)** (Scale bars: 500 μm). **(C)**: Quantification of CSPG area within the lesions of animals with transection only and with implanted polymer scaffolds. MBP debris within the lesion site of animals with transection only **(D)** and with implanted polymer scaffolds **(E)** (Scale bars: 500 μm). **(F)**: Quantification of MBP area within the lesions of animals with transection only and with implanted polymer scaffolds. Higher powered images of the deposits are shown in Supplementary Figure S5. CSPG, chondroitin sulfate proteoglycan. Color images available online at www.liebertpub.com/tea

fibroblast, macrophage, and pericyte activation in response to the polymer scaffold.[18,65,66] Few axons traversed this collagen barrier.

Previous studies in our laboratory have demonstrated that more axons are found crossing the bridging scaffold at 1 month postimplantation than at 2 months.[36] This loss of regenerated axons could be due to a lack of trophic support within the scaffold channels, as the dense collagen scarring prevents glial cells from entering. However, a drastic loss of donor GFP^+ Schwann cells was observed at 3 weeks post-implantation that could also have a negative influence on axon regeneration and viability at later time points. This loss of donor cells may be due to immune rejection of the transplanted cells, since outbred Sprague Dawley rats were used in this study. This immune reaction to the transplanted cells may also be responsible for the increased number of activated macrophages/microglia observed in the lesions of animals implanted with Schwann cell-loaded scaffolds compared with scaffolds with Matrigel only.

There was no difference in the lesion between animals with scaffolds loaded with Schwann cells or Matrigel only. When compared to animals with transection only, the polymer-implanted animals showed decreased astrocyte reactivity, CSPG and MBP deposition, collagen scarring in the cord, and cyst formation. This evidence suggests that the OPF+ polymer itself is able to influence the lesion environment, possibly by modifying macrophage/microglial responses, since increased $Iba1^+$ amoeboid cells were present in lesions of polymer-implanted animals.

It has been previously shown that macrophages derived from infiltrating hematogenous monocytes undergo increased apoptotic and necrotic cell death after phagocytosis of CNS myelin compared with resident microglia, suggesting an inability of these macrophages to efficiently degrade phagocytosed myelin.[12] However, these peripherally derived macrophages were also shown to be the predominant phagocytic cells at later times after SCI. Interestingly, the increased amoeboid $Iba1^+$ cells observed within the lesions of polymer-implanted animals in this study could signify a preservation of macrophage viability and function in the presence of the OPF+ scaffold, allowing these cells to clear inhibitory debris and preventing secondary damage within the lesion site resulting from macrophage cell death.

Iba1 expression was found to be lower on cells within the lesion site that contained substantial amounts of MBP, and more intense on cells that had not phagocytosed any MBP. This diminished Iba1 expression could represent a reduction in phagocytic activity of these cells as they process the previously engulfed MBP, since Iba1 has been shown to play an important role in the activation of microglia through the Rho GTPase Rac.[67] The increased clearance of MBP within the lesions of polymer-implanted animals could have contributed to the reduction in astrocyte reactivity, since previous studies have shown that extracellular MBP increases chemokine production and proliferation of astrocytes *in vitro*.[68,69]

We were not able to identify many of the macrophages/microglia found in the lesions of polymer-implanted animals through staining with the cell surface markers CD86 or CD206, suggesting a polarization of these cells to an unknown phenotype. However, it has been previously shown that macrophage surface markers suggesting an M1 or M2 phenotype may not correspond with the cytokine producing profile of these cells when in contact with biomaterials.[70] Therefore, it will be important in future studies to evaluate the cytokine production and mRNA profiles of these cells to determine the phenotype to which macrophages/microglia are polarized after OPF+ scaffold implantation.

As the OPF+ polymer undergoes hydrolysis over time *in vivo*, the fumaric acid byproducts that are released may also have an anti-inflammatory and neuroprotective effect, and may suppress astrocyte reactivity. Fumaric acid esters (FAE) are used in treating relapsing- remitting multiple sclerosis, and have been shown to shift leukocyte cytokine balance from T_h1 to T_h2 and activate protective antioxidant pathways in neurons and glia.[71,72] FAE have also been shown to reduce astrocyte and microglial activation and production of inflammatory cytokines.[73,74] Furthermore, the mechanical stabilization of the transected spinal cord by the OPF+ scaffold, which has similar mechanical properties to the cord,[45] may help prevent excessive scarring and cyst formation after injury.

Although the presence of Schwann cells within the scaffolds did not affect the lesion environment, previous studies in our laboratory have demonstrated that Schwann cells are crucial for axon regeneration.[36,40] Schwann cells have been shown to have an essential role in axonal regeneration after peripheral nerve injury, dedifferentiating and releasing various growth factors such as neurotrophin-3 (NT-3), nerve growth factor (NGF), brain-derived neurotrophic factor (BDNF), ciliary neurotrophic factor (CNTF), and fibroblast growth factor (FGF).[75] OPF+ was the most supportive polymer for axonal regeneration in SCI in a previous study.[45] We therefore propose that OPF+ scaffold implantation produces a more permissive lesion environment by reducing factors that inhibit axon regeneration, while Schwann cells may act on the axons directly, possibly through the production of neurotrophic factors, to reinitiate growth programs. However, the long-term foreign body response to the implanted OPF+ scaffold has also been identified as a potential physical barrier to axonal regeneration and viability, suggesting that therapies targeting this fibrotic response may allow increased regeneration leading to functional recovery after SCI.

Conclusions

In this study we have demonstrated a distinctive CNS tissue reaction to the implantation of OPF+ scaffolds after SCI. Scaffold implantation results in a more permissive lesion environment, with reduced stromal scarring, cyst formation, astrocyte reactivity, CSPG deposition, and myelin debris. This reduction in inhibitory elements is accompanied by an increase in amoeboid $Iba1^+$ cells within the lesion, suggesting an influence of the polymer on macrophage/microglial activation. Schwann cells implanted within the scaffold channels do not appear to have a significant effect on the lesion environment, and they may instead act directly on axons to reinitiate growth programs, possibly through neurotrophic factor release. Despite the benefits of OPF+ scaffold implantation described above, a remaining potential barrier to axonal regeneration and viability was identified in the fibrotic response to the scaffolds over time. The inhibition of this fibrotic response represents a promising therapeutic target to improve

the ability of these scaffolds to bridge lesions in the spinal cord and restore neurologic function.

Acknowledgments

We thank Professor Charles Howe for critical reading of the article. We thank James Tarara for his help with imaging and microscopy. We thank Jarred Nesbit and Bret Ball for their help with animal care and surgeries. We thank Jane Meyer for her administrative role in article preparation. This work was supported by grants from the NIH (EB02390, UL1TR000135), and the Morton, Kipnis, and Mayo Foundations (AJW).

Disclosure Statement

No competing financial interests exist.

References

1. CDC - Spinal Cord Injury (SCI): Fact Sheet - Traumatic Brain Injury - Injury Center. Online. 2014. Available from URL: http://www.cdc.gov/traumaticbraininjury/scifacts.html.
2. Silver, J., and Miller, J.H. Regeneration beyond the glial scar. Nat Rev Neurosci **5**, 146, 2004.
3. Davalos, D., Grutzendler, J., Yang, G., Kim, J.V., Zuo, Y., Jung, S., Littman, D.R., Dustin, M.L., and Gan, W.B. ATP mediates rapid microglial response to local brain injury in vivo. Nat Neurosci **8**, 752, 2005.
4. Stence, N., Waite, M., and Dailey, M.E. Dynamics of microglial activation: a confocal time-lapse analysis in hippocampal slices. Glia **33**, 256, 2001.
5. Dibaj, P., Nadrigny, F., Steffens, H., Scheller, A., Hirrlinger, J., Schomburg, E.D., Neusch, C., and Kirchhoff, F. NO mediates microglial response to acute spinal cord injury under ATP control in vivo. Glia **58**, 1133, 2010.
6. Bartholdi, D., and Schwab, M.E. Expression of pro-inflammatory cytokine and chemokine mRNA upon experimental spinal cord injury in mouse: an in situ hybridization study. Eur J Neurosci **9**, 1422, 1997.
7. Chen, M.S., Huber, A.B., van der Haar, M.E., Frank, M., Schnell, L., Spillmann, A.A., Christ, F., and Schwab, M.E. Nogo-A is a myelin-associated neurite outgrowth inhibitor and an antigen for monoclonal antibody IN-1. Nature **403**, 434, 2000.
8. McKerracher, L., David, S., Jackson, D.L., Kottis, V., Dunn, R.J., and Braun, P.E. Identification of myelin-associated glycoprotein as a major myelin-derived inhibitor of neurite growth. Neuron **13**, 805, 1994.
9. Mukhopadhyay, G., Doherty, P., Walsh, F.S., Crocker, P.R., and Filbin, M.T. A novel role for myelin-associated glycoprotein as an inhibitor of axonal regeneration. Neuron **13**, 757, 1994.
10. Cafferty, W.B., Duffy, P., Huebner, E., and Strittmatter, S.M. MAG and OMgp synergize with Nogo-A to restrict axonal growth and neurological recovery after spinal cord trauma. J Neurosci **30**, 6825, 2010.
11. Imai, M., Watanabe, M., Suyama, K., Osada, T., Sakai, D., Kawada, H., Matsumae, M., and Mochida, J. Delayed accumulation of activated macrophages and inhibition of remyelination after spinal cord injury in an adult rodent model. J Neurosurg Spine **8**, 58, 2008.
12. Greenhalgh, A.D., and David, S. Differences in the phagocytic response of microglia and peripheral macrophages after spinal cord injury and its effects on cell death. J Neurosci **34**, 6316, 2014.
13. Hu, R., Zhou, J., Luo, C., Lin, J., Wang, X., Li, X., Bian, X., Li, Y., Wan, Q., Yu, Y., and Feng, H. Glial scar and neuroregeneration: histological, functional, and magnetic resonance imaging analysis in chronic spinal cord injury. J Neurosurg Spine **13**, 169, 2010.
14. Bush, T.G., Puvanachandra, N., Horner, C.H., Polito, A., Ostenfeld, T., Svendsen, C.N., Mucke, L., Johnson, M.H., and Sofroniew, M.V. Leukocyte infiltration, neuronal degeneration, and neurite outgrowth after ablation of scar-forming, reactive astrocytes in adult transgenic mice. Neuron **23**, 297, 1999.
15. McKeon, R.J., Hoke, A., and Silver, J. Injury-induced proteoglycans inhibit the potential for laminin-mediated axon growth on astrocytic scars. Exp Neurol **136**, 32, 1995.
16. McKeon, R.J., Schreiber, R.C., Rudge, J.S., and Silver, J. Reduction of neurite outgrowth in a model of glial scarring following CNS injury is correlated with the expression of inhibitory molecules on reactive astrocytes. J Neurosci **11**, 3398, 1991.
17. Rudge, J.S., and Silver, J. Inhibition of neurite outgrowth on astroglial scars in vitro. J Neurosci **10**, 3594, 1990.
18. Goritz, C., Dias, D.O., Tomilin, N., Barbacid, M., Shupliakov, O., and Frisen, J. A pericyte origin of spinal cord scar tissue. Science **333**, 238, 2011.
19. Tang, X., Davies, J.E., and Davies, S.J. Changes in distribution, cell associations, and protein expression levels of NG2, neurocan, phosphacan, brevican, versican V2, and tenascin-C during acute to chronic maturation of spinal cord scar tissue. J Neurosci Res **71**, 427, 2003.
20. De Winter, F., Oudega, M., Lankhorst, A.J., Hamers, F.P., Blits, B., Ruitenberg, M.J., Pasterkamp, R.J., Gispen, W.H., and Verhaagen, J. Injury-induced class 3 semaphorin expression in the rat spinal cord. Exp Neurol **175**, 61, 2002.
21. Soderblom, C., Luo, X., Blumenthal, E., Bray, E., Lyapichev, K., Ramos, J., Krishnan, V., Lai-Hsu, C., Park, K.K., Tsoulfas, P., and Lee, J.K. Perivascular fibroblasts form the fibrotic scar after contusive spinal cord injury. J Neurosci **33**, 13882, 2013.
22. Lindholm, D., Castren, E., Kiefer, R., Zafra, F., and Thoenen, H. Transforming growth factor-beta 1 in the rat brain: increase after injury and inhibition of astrocyte proliferation. J Cell Biol **117**, 395, 1992.
23. Logan, A., Green, J., Hunter, A., Jackson, R., and Berry, M. Inhibition of glial scarring in the injured rat brain by a recombinant human monoclonal antibody to transforming growth factor-beta2. Eur J Neurosci **11**, 2367, 1999.
24. Shi, Q., Gao, W., Han, X., Zhu, X., Sun, J., Xie, F., Hou, X., Yang, H., Dai, J., and Chen, L. Collagen scaffolds modified with collagen-binding bFGF promotes the neural regeneration in a rat hemisected spinal cord injury model. Sci China Life Sci **57**, 232, 2014.
25. Silva, N.A., Salgado, A.J., Sousa, R.A., Oliveira, J.T., Pedro, A.J., Leite-Almeida, H., Cerqueira, R., Almeida, A., Mastronardi, F., Mano, J.F., Neves, N.M., Sousa, N., and Reis, R.L. Development and characterization of a novel hybrid tissue engineering-based scaffold for spinal cord injury repair. Tissue Eng Part A **16**, 45, 2010.
26. Jain, A., Kim, Y.T., McKeon, R.J., and Bellamkonda, R.V. In situ gelling hydrogels for conformal repair of spinal cord defects, and local delivery of BDNF after spinal cord injury. Biomaterials **27**, 497, 2006.

27. De Laporte, L., Yan, A.L., and Shea, L.D. Local gene delivery from ECM-coated poly(lactide-co-glycolide) multiple channel bridges after spinal cord injury. Biomaterials **30**, 2361, 2009.
28. Pertici, V., Trimaille, T., Laurin, J., Felix, M.S., Marqueste, T., Pettmann, B., Chauvin, J.P., Gigmes, D., and Decherchi, P. Repair of the injured spinal cord by implantation of a synthetic degradable block copolymer in rat. Biomaterials 2014.
29. Petter-Puchner, A.H., Froetscher, W., Krametter-Froetscher, R., Lorinson, D., Redl, H., and van Griensven, M. The long-term neurocompatibility of human fibrin sealant and equine collagen as biomatrices in experimental spinal cord injury. Exp Toxicol Pathol **58**, 237, 2007.
30. Mothe, A.J., Tam, R.Y., Zahir, T., Tator, C.H., and Shoichet, M.S. Repair of the injured spinal cord by transplantation of neural stem cells in a hyaluronan-based hydrogel. Biomaterials **34**, 3775, 2013.
31. Ritfeld, G.J., Rauck, B.M., Novosat, T.L., Park, D., Patel, P., Roos, R.A., Wang, Y., and Oudega, M. The effect of a polyurethane-based reverse thermal gel on bone marrow stromal cell transplant survival and spinal cord repair. Biomaterials **35**, 1924, 2014.
32. Runge, M.B., Dadsetan, M., Baltrusaitis, J., Ruesink, T., Lu, L., Windebank, A.J., and Yaszemski, M.J. Development of electrically conductive oligo(polyethylene glycol) fumarate-polypyrrole hydrogels for nerve regeneration. Biomacromolecules **11**, 2845, 2010.
33. Kim, J., Dadsetan, M., Ameenuddin, S., Windebank, A.J., Yaszemski, M.J., and Lu, L. In vivo biodegradation and biocompatibility of PEG/sebacic acid-based hydrogels using a cage implant system. J Biomed Mater Res A **95**, 191, 2010.
34. Krych, A.J., Rooney, G.E., Chen, B., Schermerhorn, T.C., Ameenuddin, S., Gross, L., Moore, M.J., Currier, B.L., Spinner, R.J., Friedman, J.A., Yaszemski, M.J., and Windebank, A.J. Relationship between scaffold channel diameter and number of regenerating axons in the transected rat spinal cord. Acta Biomater **5**, 2551, 2009.
35. Dadsetan, M., Knight, A.M., Lu, L., Windebank, A.J., and Yaszemski, M.J. Stimulation of neurite outgrowth using positively charged hydrogels. Biomaterials **30**, 3874, 2009.
36. Chen, B.K., Knight, A.M., de Ruiter, G.C., Spinner, R.J., Yaszemski, M.J., Currier, B.L., and Windebank, A.J. Axon regeneration through scaffold into distal spinal cord after transection. J Neurotrauma **26**, 1759, 2009.
37. Olson, H.E., Rooney, G.E., Gross, L., Nesbitt, J.J., Galvin, K.E., Knight, A., Chen, B., Yaszemski, M.J., and Windebank, A.J. Neural stem cell- and Schwann cell-loaded biodegradable polymer scaffolds support axonal regeneration in the transected spinal cord. Tissue Eng Part A **15**, 1797, 2009.
38. de Ruiter, G.C., Onyeneho, I.A., Liang, E.T., Moore, M.J., Knight, A.M., Malessy, M.J., Spinner, R.J., Lu, L., Currier, B.L., Yaszemski, M.J., and Windebank, A.J. Methods for in vitro characterization of multichannel nerve tubes. J Biomed Mater Res A **84**, 643, 2008.
39. Jabbari, E., Wang, S., Lu, L., Gruetzmacher, J.A., Ameenuddin, S., Hefferan, T.E., Currier, B.L., Windebank, A.J., and Yaszemski, M.J. Synthesis, material properties, and biocompatibility of a novel self-cross-linkable poly(caprolactone fumarate) as an injectable tissue engineering scaffold. Biomacromolecules **6**, 2503, 2005.
40. Moore, M.J., Friedman, J.A., Lewellyn, E.B., Mantila, S.M., Krych, A.J., Ameenuddin, S., Knight, A.M., Lu, L., Currier, B.L., Spinner, R.J., Marsh, R.W., Windebank, A.J., and Yaszemski, M.J. Multiple-channel scaffolds to promote spinal cord axon regeneration. Biomaterials **27**, 419, 2006.
41. Friedman, J.A., Windebank, A.J., Moore, M.J., Spinner, R.J., Currier, B.L., and Yaszemski, M.J. Biodegradable polymer grafts for surgical repair of the injured spinal cord. Neurosurgery **51**, 742, 2002.
42. Rooney, G.E., Knight, A.M., Madigan, N.N., Gross, L., Chen, B., Giraldo, C.V., Seo, S., Nesbitt, J.J., Dadsetan, M., Yaszemski, M.J., and Windebank, A.J. Sustained delivery of dibutyryl cyclic adenosine monophosphate to the transected spinal cord via oligo [(polyethylene glycol) fumarate] hydrogels. Tissue Eng Part A **17**, 1287, 2011.
43. Rooney, G.E., Vaishya, S., Ameenuddin, S., Currier, B.L., Schiefer, T.K., Knight, A., Chen, B., Mishra, P.K., Spinner, R.J., Macura, S.I., Yaszemski, M.J., and Windebank, A.J. Rigid fixation of the spinal column improves scaffold alignment and prevents scoliosis in the transected rat spinal cord. Spine **33**, E914, 2008.
44. Daly, W.T., Knight, A.M., Wang, H., de Boer, R., Giusti, G., Dadsetan, M., Spinner, R.J., Yaszemski, M.J., and Windebank, A.J. Comparison and characterization of multiple biomaterial conduits for peripheral nerve repair. Biomaterials **34**, 8630, 2013.
45. Chen, B.K., Knight, A.M., Madigan, N.N., Gross, L., Dadsetan, M., Nesbitt, J.J., Rooney, G.E., Currier, B.L., Yaszemski, M.J., Spinner, R.J., and Windebank, A.J. Comparison of polymer scaffolds in rat spinal cord: a step toward quantitative assessment of combinatorial approaches to spinal cord repair. Biomaterials **32**, 8077, 2011.
46. Anderson, J.M., Rodriguez, A., and Chang, D.T. Foreign body reaction to biomaterials. Semin Immunol **20**, 86, 2008.
47. Brown, B.N., Ratner, B.D., Goodman, S.B., Amar, S., and Badylak, S.F. Macrophage polarization: an opportunity for improved outcomes in biomaterials and regenerative medicine. Biomaterials **33**, 3792, 2012.
48. Franz, S., Rammelt, S., Scharnweber, D., and Simon, J.C. Immune responses to implants - a review of the implications for the design of immunomodulatory biomaterials. Biomaterials **32**, 6692, 2011.
49. Shechter, R., Miller, O., Yovel, G., Rosenzweig, N., London, A., Ruckh, J., Kim, K.W., Klein, E., Kalchenko, V., Bendel, P., Lira, S.A., Jung, S., and Schwartz, M. Recruitment of beneficial M2 macrophages to injured spinal cord is orchestrated by remote brain choroid plexus. Immunity **38**, 555, 2013.
50. Kigerl, K.A., Gensel, J.C., Ankeny, D.P., Alexander, J.K., Donnelly, D.J., and Popovich, P.G. Identification of two distinct macrophage subsets with divergent effects causing either neurotoxicity or regeneration in the injured mouse spinal cord. J Neurosci **29**, 13435, 2009.
51. Rapalino, O., Lazarov-Spiegler, O., Agranov, E., Velan, G.J., Yoles, E., Fraidakis, M., Solomon, A., Gepstein, R., Katz, A., Belkin, M., Hadani, M., and Schwartz, M. Implantation of stimulated homologous macrophages results in partial recovery of paraplegic rats. Nat Med **4**, 814, 1998.
52. Shechter, R., London, A., Varol, C., Raposo, C., Cusimano, M., Yovel, G., Rolls, A., Mack, M., Pluchino, S., Martino, G., Jung, S., and Schwartz, M. Infiltrating blood-derived macrophages are vital cells playing an anti-inflammatory role in recovery from spinal cord injury in mice. PLoS Med **6**, e1000113, 2009.
53. Yin, Y., Henzl, M.T., Lorber, B., Nakazawa, T., Thomas, T.T., Jiang, F., Langer, R., and Benowitz, L.I. Oncomo-

dulin is a macrophage-derived signal for axon regeneration in retinal ganglion cells. Nat Neurosci **9**, 843, 2006.
54. Anderson, J.M., and Jones, J.A. Phenotypic dichotomies in the foreign body reaction. Biomaterials **28**, 5114, 2007.
55. Gaudet, A.D., Popovich, P.G., and Ramer, M.S. Wallerian degeneration: gaining perspective on inflammatory events after peripheral nerve injury. J Neuroinflammation **8**, 110, 2011.
56. Rotshenker, S. Wallerian degeneration: the innate-immune response to traumatic nerve injury. J Neuroinflammation **8**, 109, 2011.
57. Dadsetan, M., Szatkowski, J.P., Yaszemski, M.J., and Lu, L. Characterization of photo-cross-linked oligo[poly(ethylene glycol) fumarate] hydrogels for cartilage tissue engineering. Biomacromolecules **8**, 1702, 2007.
58. Dadsetan, M., Liu, Z., Pumberger, M., Giraldo, C.V., Ruesink, T., Lu, L., and Yaszemski, M.J. A stimuli-responsive hydrogel for doxorubicin delivery. Biomaterials **31**, 8051, 2010.
59. Shin, H., Quinten Ruhé, P., Mikos, A.G., and Jansen, J.A. In vivo bone and soft tissue response to injectable, biodegradable oligo(poly(ethylene glycol) fumarate) hydrogels. Biomaterials **24**, 3201, 2003.
60. Jo, S., Shin, H., Shung, A.K., Fisher, J.P., and Mikos, A.G. Synthesis and characterization of oligo(poly(ethylene glycol) fumarate) macromer. Macromolecules **34**, 2839, 2001.
61. Kinard, L.A., Kasper, F.K., and Mikos, A.G. Synthesis of oligo(poly(ethylene glycol) fumarate). Nature protocols **7**, 1219, 2012.
62. Dadsetan, M., Pumberger, M., Casper, M.E., Shogren, K., Giuliani, M., Ruesink, T., Hefferan, T.E., Currier, B.L., and Yaszemski, M.J. The effects of fixed electrical charge on chondrocyte behavior. Acta biomaterialia **7**, 2080, 2011.
63. Rooney, G.E., Moran, C., McMahon, S.S., Ritter, T., Maenz, M., Flugel, A., Dockery, P., O'Brien, T., Howard, L., Windebank, A.J., and Barry, F.P. Gene-modified mesenchymal stem cells express functionally active nerve growth factor on an engineered poly lactic glycolic acid (PLGA) substrate. Tissue Eng Part A **14**, 681, 2008.
64. Kettenmann, H., Hanisch, U.K., Noda, M., and Verkhratsky, A. Physiology of microglia. Physiol Rev **91**, 461, 2011.
65. Kawano, H., Kimura-Kuroda, J., Komuta, Y., Yoshioka, N., Li, H.P., Kawamura, K., Li, Y., and Raisman, G. Role of the lesion scar in the response to damage and repair of the central nervous system. Cell Tissue Res **349**, 169, 2012.
66. Klapka, N., and Muller, H.W. Collagen matrix in spinal cord injury. J Neurotrauma **23**, 422, 2006.
67. Imai, Y., and Kohsaka, S. Intracellular signaling in M-CSF-induced microglia activation: role of Iba1. Glia **40**, 164, 2002.
68. Calderon, T.M., Eugenin, E.A., Lopez, L., Kumar, S.S., Hesselgesser, J., Raine, C.S., and Berman, J.W. A role for CXCL12 (SDF-1alpha) in the pathogenesis of multiple sclerosis: regulation of CXCL12 expression in astrocytes by soluble myelin basic protein. J Neuroimmunol **177**, 27, 2006.
69. South, S.A., Deibler, G.E., Tzeng, S.F., Badache, A., Kirchner, M.G., Muja, N., and De Vries, G.H. Myelin basic protein (MBP) and MBP peptides are mitogens for cultured astrocytes. Glia **29**, 81, 2000.
70. Bartneck, M., Heffels, K.H., Pan, Y., Bovi, M., Zwadlo-Klarwasser, G., and Groll, J. Inducing healing-like human primary macrophage phenotypes by 3D hydrogel coated nanofibres. Biomaterials **33**, 4136, 2012.
71. Linker, R.A., and Gold, R. Dimethyl fumarate for treatment of multiple sclerosis: mechanism of action, effectiveness, and side effects. Current neurology and neuroscience reports **13**, 394, 2013.
72. Albrecht, P., Bouchachia, I., Goebels, N., Henke, N., Hofstetter, H.H., Issberner, A., Kovacs, Z., Lewerenz, J., Lisak, D., Maher, P., Mausberg, A.K., Quasthoff, K., Zimmermann, C., Hartung, H.P., and Methner, A. Effects of dimethyl fumarate on neuroprotection and immunomodulation. J Neuroinflammation **9**, 163, 2012.
73. Wierinckx, A., Breve, J., Mercier, D., Schultzberg, M., Drukarch, B., and Van Dam, A.M. Detoxication enzyme inducers modify cytokine production in rat mixed glial cells. J Neuroimmunol **166**, 132, 2005.
74. Lin, S.X., Lisi, L., Dello Russo, C., Polak, P.E., Sharp, A., Weinberg, G., Kalinin, S., and Feinstein, D.L. The anti-inflammatory effects of dimethyl fumarate in astrocytes involve glutathione and haem oxygenase-1. ASN Neuro **3**, 2011.
75. Willerth, S.M., and Sakiyama-Elbert, S.E. Cell therapy for spinal cord regeneration. Adv Drug Deliv Rev **60**, 263, 2008.

Address correspondence to:
Anthony J. Windebank, MD
Department of Neurology
Mayo Clinic
200 First Street SW
Rochester, MN 55905

E-mail: windebank.anthony@mayo.edu

Received: January 14, 2015
Accepted: March 23, 2015
Online Publication Date: June 15, 2015